

Modeling self-assembled quantum dots by the effective bond-orbital method

Sophia J. Sun and Yia-Chung Chang

Department of Physics and Materials Research Laboratory University of Illinois at Urbana-Champaign, Urbana, Illinois 61801

(Received 2 June 2000)

Systematic studies of the electronic and optical properties of InAs/GaAs self-assembled quantum dots are performed via the effective bond-orbital model employed with an efficient algorithm. Four different sizes of pyramid and one truncated pyramid with $\{110\}$ sidewall quantum dots (QD's) are studied. Microscopic strain distributions have been taken into account via valence-force-field model. We find that charge density distribution and optical properties are quite different with and without including the piezoelectric effect. Without the piezoelectric effect, variation in dot size can lead to a substantial change in the strain distribution and hence the charge distribution, which gives rise to qualitatively different optical properties. Including the piezoelectric effect, hole-state wave functions are stretched along the $[1\bar{1}0]$ axis and hence interband optical transitions become polarized along $[1\bar{1}0]$ and the polarization ratio increases with dot size. Our results of the energy levels and optical polarization are in good agreement with experimental and other theoretical results. Our calculations of truncated pyramid QD's indicate that the truncation of the pyramid tip has a negligible effect on the photoluminescence properties of QD's.

I. INTRODUCTION

Defect-free coherent nanoscale islands fabricated by the Stranski-Krastanow method, known as self-assembled quantum dots (SAQD's), have attracted scientific interest recently due to their potential applications in optoelectronic devices, such as low-threshold lasers and novel infrared detectors.¹⁻⁴ In the last decade, a tremendous attraction has been shown to studies of SAQD's both from a basic physical interest and for practical applications. Most of these work focus on the formation and characterization and electronic and optical properties of SAQD's.⁵⁻²⁷ The size fluctuation of SAQD's hampers the experimental investigations of the excited-state spectrum and brings difficulties in the comparison between experimental and theoretical results. Recently much effort has been devoted to this issue and new experimental techniques with high spatial resolution and sensitivity such as near-field scanning optical microscopy (NSOM) and Cathode luminescence¹⁸ (CL) have been developed, which make the study of the electronic properties of isolated quantum dots possible.^{28,29}

In order to obtain high-performance QD devices, it is important to have a detailed understanding of the optical properties of QD's and their dependence on the dot morphology and growth condition. A recent low-temperature spectrum of isolated SAQD's exhibits rich fine structure and an unambiguous assignment of these transitions has not been available. Therefore further extensive studies on the electronic and optical properties of SAQD's with different shapes and sizes are still needed.

Current theoretical methods applied to SAQD's include the single-band or multiband effective mass method,¹⁹⁻²¹ $\mathbf{k}\cdot\mathbf{p}$ ²³⁻²⁷ and empirical pseudopotential methods.²² All these methods have their advantages and disadvantages. The effective-mass and $\mathbf{k}\cdot\mathbf{p}$ methods are most convenient to use, but they quickly become cumbersome when the full boundary conditions needed to take into account the differences in

band parameters between different materials across the interfaces for a complicated geometry (e.g., pyramidal QD) are included. The empirical pseudopotential methods can take into account the boundary conditions automatically by using atomic pseudopotentials appropriate for different atomic species at the designated positions in the QD structure and it takes into account the full band structure effects. However, the basis set needed to obtain a convergent solution to the electronic states is very large, which makes the computation of a large QD extremely time consuming. Furthermore, it is difficult to find the appropriate atomic pseudopotentials that produce the correct overall band structures for the constituent bulk materials and at the same time give effective masses for all bands near the zone center with the desired precision. For example, the pseudopotentials used in existing calculations²² give an effective mass of $0.092m_0$ for GaAs and $0.032m_0$ for InAs, which are off from the experimental values by more than 30%.

In this paper we present a theoretical study of the electronic structure and optical properties of SAQD's with a high accuracy and efficiency via the effective bond-orbital model (EBOM).³⁰ The bond-orbital model is basically a tight-binding model which uses bonding and antibonding orbitals as the basis. It is capable of taking into account the full band structure effect when a full set of bonding and antibonding orbitals (typically four for conduction bands and four for valence bands for III-V semiconductors) is used and a sufficient range of interactions between bond orbitals is considered. However, to achieve a high efficiency we adopt an effective bond-orbital model which uses a minimum basis set that includes one s -like antibonding orbital for the conduction band and three p -like bonding orbitals for the valence band and only nearest-neighbor interactions are included. The interactions between the four bond orbitals are determined by requiring the band structures of constituent bulk materials near the zone center to be identical to those obtained by the $\mathbf{k}\cdot\mathbf{p}$ theory. Thus, the model is equivalent to the real-space version of the $\mathbf{k}\cdot\mathbf{p}$ model. In addition, it offers

the flexibility to include the full band structure if needed by expanding the range of interactions between bond orbitals and it can take into account the change of the bonding nature at the interfaces between constituent materials by using appropriate interaction parameters. This model has been successfully applied to quantum wells³¹ (QW's) and quantum wires (QWR's) either grown by chemical etching³² or by the strain-induced lateral-layer ordering (SILO) process.³³

Combining the EBOM with an efficient algorithm allows us to study the electronic properties of large-size SAQD's reliably. Numerical solutions of energy eigenvalues with an accuracy better than 10^{-6} eV for a system of 10^6 atoms can be achieved on a 500 MHz DEC alphastation and the CPU time for obtaining the wave function of a given conduction-band (CB) or valence-band (VB) state is less than 5 or 8 h with our method. Widely varying shapes of SAQD's have been reported including pyramid, truncated pyramid, cone, or lens. Since pyramidal dots with $\{110\}$ sidewall are mostly studied, we apply our method to this kind of dot so that we can make a meaningful comparison with previous calculations. Four different sizes of pyramidal QD's with base lengths equal to 125, 158, 204, and 250 Å are studied. Furthermore, we also present calculations on a QD with a truncated pyramidal shape.

The organization of this paper is as follows. In Sec. II, we briefly introduce our theoretical method. In Sec. III we present our results and discussions. In Sec. IV a brief summary is given.

II. THEORETICAL METHODS

A. Valence-force-field model for strain distribution

The electronic states of SAQD depend strongly on the strain distribution. There are two methods to solve the strain distribution in QD's: the continuum mechanical (CM) model and valence-force-field (VFF) model. Pryor *et al.*³⁴ and Stier *et al.*²⁶ compared the results obtained by these two models. They found that the differences at the interfaces are largest while in the interior of QD's the differences are insignificant. Since the VFF model can give a strain tensor on the atomistic level, avoid potential failure at the interface, and retain the correct point symmetry of the system, we chose to use the VFF model in favor of the CM model. Furthermore, since both the VFF model and the effective bond-orbital model deal with the interactions between chemical bonds, the combination of the two models represents a perfect marriage of the lattice property and electronic property.

In the VFF model of Keating³⁵ and Martin,³⁶ the lattice energy of the system is described by the sum of bond stretching and bond bending terms, which takes the form

$$V = \frac{1}{4} \sum_{ij} \frac{3}{4} \alpha_{ij} (R_{ij}^2 - R_{0,ij}^2)^2 / R_{0,ij}^2 + \frac{1}{4} \sum_i \sum_{j \neq k} \frac{3}{4} \beta_{ijk} (\mathbf{R}_{ij} \cdot \mathbf{R}_{ik} + R_{0,ij} R_{0,ik} / 3)^2 / R_{0,ij} R_{0,ik}, \quad (1)$$

where i runs over all the atom positions j and k run over the nearest-neighbor sites of i , \mathbf{R}_{ij} is the vector joining the sites i and j , R_{ij} is the length of the bond, $R_{0,ij}$ is the corresponding equilibrium length in the binary constituents, and α_{ij} and β_{ijk} are the bond-stretching and bond-bending constants, re-

spectively. α and β of the binary constituent component are from Martin's calculations.³⁶ For the bond-bending parameter β of In-Ga-As, we take $\beta_{ijk} = \sqrt{\beta_{ij}\beta_{ik}}$ following Ref. 25.

To calculate the strain tensor, we used an efficient method to minimize the potential energy given above. Since the systems contain more than 10^5 atoms, it is impractical to directly solve the equation $\partial V / \partial \mathbf{R} = 0$. We first place the atoms on the ideal lattice of bulk GaAs; then we allow atoms to be displaced from these ideal positions and in each iteration only one atom is displaced while others are fixed. The displacement of atom i is determined according to the force $f_i = -\partial V / \partial x_i$ with periodic boundary conditions in the plane perpendicular to the growth direction. We repeat this process until the force acting on each atom becomes zero.

Once the equilibrium is reached, the strain tensor is calculated according to the method described in Ref. 34, namely,

$$\boldsymbol{\varepsilon} = \mathbf{R} \begin{pmatrix} R_{0,12x} & R_{0,23x} & R_{0,34x} \\ R_{0,12y} & R_{0,23y} & R_{0,34y} \\ R_{0,12z} & R_{0,23z} & R_{0,34z} \end{pmatrix}^{-1} - I, \quad (2)$$

where I is the unity matrix, $R_{0,ij} = R_{0,j} - R_{0,i}$, $i, j = 1, 4$, and $R_{0,i}$ ($i = 1, 4$) denotes the positions of the four As atoms surrounding a cation. Here we chose $R_{0,12} = (1, -1, 0)a/2$, $R_{0,23} = (-1, 0, 1)a/2$, and $R_{0,34} = (1, 1, 0)a/2$, where a is the lattice constant of GaAs or InAs, depending on the site.

B. EBOM for electronic states

The energy levels and wave functions of the capped pyramidal self-assemble quantum dots are calculated in the effective bond-orbital model. A detailed description of this method can be found in Refs. 30, 37 and 38. The EBOM used here is a tight-binding-like model in which one s -like conduction band and three p -like valence bands (before including the spin-orbit interaction) are coupled. After including the spin-orbit interaction, we have two conduction bands and six valence bands. Thus, the present model should be compared with the eight-band $\mathbf{k} \cdot \mathbf{p}$ model as used in Ref. 26. To estimate the effects of the piezoelectric charge induced by the shear strain, we also included the piezoelectric potential. The piezoelectric potential at site \mathbf{R} in the EBOM is given by

$$V_p(\mathbf{R}) = - \sum_{\mathbf{R}'} \frac{e \rho_p(\mathbf{R}')}{\epsilon_0 |\mathbf{R} - \mathbf{R}'|},$$

where e is the electron charge, ϵ_0 is the static dielectric constant, and $\rho_p(\mathbf{R}')$ is the piezoelectric charge at site \mathbf{R}' . Due to the singularity of the Coulomb interaction at the origin (when $\mathbf{R}' = \mathbf{R}$), we approximate the denominator $|\mathbf{R} - \mathbf{R}'|$ by an effective interaction length r_0 , which is taken to be half of the bond length. Since $\rho_p(\mathbf{R}')$ is a smooth function of \mathbf{R}' , the result is insensitive to the value of r_0 .

The Hamiltonian for p -like valence band states (before including the spin-orbit interaction) has the form

TABLE I. Parameters used in the present work (in units of eV).

Parameters	GaAs	InAs
CB minimum ^a	1.495	0.662
VB maximum ^b	0.0	0.26
Spin-orbital coupling ^a	0.34	0.38
Deformation potentials ^b		
a_c	-7.17	-5.08
a_v	-1.16	-1.00
b	-1.6	-1.8
d	-4.23	-3.1

^aReference 44.^bReference 43.

$$H_{\alpha,\alpha'} = (E_p + V_p) \delta_{\alpha,\alpha'} + \sum_{\tau} \exp^{i\mathbf{k} \cdot \boldsymbol{\tau}} \{E_{xy} \tau_{\alpha} \tau_{\alpha'} + [(E_{xx} - E_{xy}) \tau_{\alpha}^2 + E_{zz} (1 - \tau_{\alpha}^2)] \delta_{\alpha,\alpha'}\} + H_{st}, \quad (3)$$

where $\tau_{\alpha} = (2/a)R_{0,\alpha}$; $\alpha = x, y, z$ are dimensionless components of the four lattice vectors defined above. The interaction parameters E_p , E_{xx} , E_{xy} , and E_{zz} can be directly related to the $\mathbf{k} \cdot \mathbf{p}$ band parameters and the analytical relations can be found in Ref. 30. V_p is the piezoelectric potential, and H_{st} is the strain Hamiltonian. Because H only couples sites separated by a nearest-neighbor distance, the number of non-zero matrix elements of H needed to be stored is linearly proportional to the number of atoms in the system (N). Thus, our algorithm scales like order N .

With the strain tensor ε_{ij} calculated according to the VFF model as described above, the strain Hamiltonian is related to ε_{ij} according to Bir-Pikus theory.³⁹ For the VB states we have

$$H_{st} = \begin{pmatrix} -\Delta V_H + D_1 & \sqrt{3}de_{xy} & \sqrt{3}de_{xz} \\ \sqrt{3}de_{xy} & -\Delta V_H + D_2 & \sqrt{3}de_{yz} \\ \sqrt{3}de_{xz} & \sqrt{3}de_{yz} & -\Delta V_H + D_3 \end{pmatrix}, \quad (4)$$

where $e_{ij} = (\varepsilon_{ij} + \varepsilon_{ji})/2$, $\Delta V_H = (a_1 + a_2)(\varepsilon_{xx} + \varepsilon_{yy} + \varepsilon_{zz})$, $D_1 = b(2\varepsilon_{xx} - \varepsilon_{yy} - \varepsilon_{zz})$, $D_2 = b(2\varepsilon_{yy} - \varepsilon_{xx} - \varepsilon_{zz})$, and $D_3 = d(2\varepsilon_{zz} - \varepsilon_{xx} - \varepsilon_{yy})$. Here a_1 , a_2 , b , and d are deformation potentials listed in Table I.

The Hamiltonian for the s -like conduction band is $H_s = E_s + V_p + c_1(\varepsilon_{xx} + \varepsilon_{yy} + \varepsilon_{zz})$, where E_s is the on-site orbital energy for the s -like orbital, V_p is the piezoelectric potential, and c_1 is the CB deformation potential. The coupling between s -like and p -like bond orbitals is given by $\langle s|H|\alpha, \mathbf{R}_0\rangle = E_{sp} \tau_{\alpha}$.

In order to solve the single electron Schrödinger equation of the system containing more than 10^5 atoms efficiently, we adopt a three-step procedure. In the first step, we decouple the CB and VB states and use a conjugate gradient method to find the low-lying eigenstates of H_s for the CB and high-lying eigenstates of H_p for the VB for a given symmetry type. Here we utilize the C_{2v} symmetry of SAQD's and require the eigenstates to transform according to the A_1 , A_2 , B_1 , or B_2 representation. Here and henceforth, we adopt the

group theory notation of Ref. 40. The four elements of the C_{2v} group are E (identity), σ_v (mirror plane normal to the $[1\bar{1}0]$ direction or the x' axis), $\sigma_{v'}$ (mirror plane normal to the $[110]$ direction or the y' axis), and C_2 (twofold rotation about the $[001]$ axis). For example, to find the highest-lying VB state with A_1 symmetry, we first make an initial guess of the wave function denoted $C_{\alpha}(\mathbf{R})$ for \mathbf{R} in a quadrant of the QD unit cell. We then require the wave function for \mathbf{R} in the three other quadrants to be related to $C_{\alpha}(\mathbf{R})$ by applying the three symmetry operations σ_v , $\sigma_{v'}$, and C_2 . The wave function is updated each iteration along the gradient of the potential defined as $f = -2(H - \langle E \rangle)C$, where $\langle E \rangle = C^{\dagger}HC$. Since all matrix elements are real at this stage, we have C^{\dagger} equal to the transpose of C . To find the excited states of the same symmetry type, we repeat the above procedure, but with the added constraint that requires the state to be orthogonal to the states previously solved.

In the second step we find the eigenstate of the CB-VB coupled Hamiltonian using the eigenstates of the decoupled Hamiltonian obtained in step 1 as the initial guess. At this step the energy of interest falls in the middle of the spectrum for the coupled Hamiltonian, and we can no longer use the conjugate gradient method here. Since our initial guess is already a good approximation to the final answer, we can find the accurate eigenstate by simply inverting the Schrödinger equation. We shall refer to this method as the inverse Schrödinger equation (ISE) method. Our ISE method goes as follows. We write the Schrödinger equation in the form

$$\sum_{n' \neq n} \langle n|H|n'\rangle C_{n'} + \langle n|H|n\rangle C_n = E C_n, \quad (5)$$

where n (or n') is a composite label for site and orbital (\mathbf{R}, α). Inverting the above equation, we have

$$C_n = \sum_{n' \neq n} \langle n|H|n'\rangle C_{n'} / (E - \langle n|H|n\rangle), \quad (6)$$

with $E = C^{\dagger}HC$.

The above recursion relation is solved by iteration until the self-consistency is reached. It turns out that the ISE method converges very fast as long as the initial guess is good enough. For electron ground states of all cases considered here, within 1000 iterations a convergence in the energy eigenvalue better than 10^{-6} eV can be achieved.

In the third step, we include the spin-orbital interaction. The total Hamiltonian including the spin-orbit interaction takes the form

$$H = \begin{pmatrix} H_u + U_{so} & V_{so} \\ V_{so}^{\dagger} & H_d - U_{so} \end{pmatrix}, \quad (7)$$

where H_u and H_d are Hamiltonians for spin-up and spin-down components, each being identical to the one used in step 2. Here U_{so} and V_{so} describe the spin-orbital interaction between states of the same spin and opposite spin. The non-zero matrix elements are⁴¹ $\langle x|U_{so}|y\rangle = -\langle y|U_{so}|x\rangle = -i\Delta/3$, $\langle x|V_{so}|z\rangle = -\langle z|V_{so}|x\rangle = \Delta/3$, and $\langle y|V_{so}|z\rangle = -\langle z|V_{so}|y\rangle = -i\Delta/3$, where Δ is the spin-orbit splitting for valence band states. All spin-orbit coupled states transform

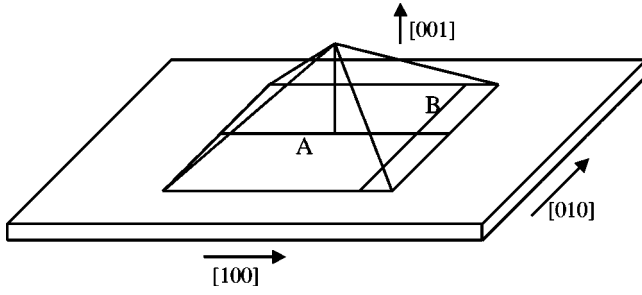


FIG. 1. Schematic plot of the pyramidal dot and wetting layer geometry. z is the growth direction, x is $[100]$, and y is $[010]$.

according to the double group representation of C_{2v} . The spin-up and spin-down states have the form⁴²

$$\psi_{1/2} = (|A_1\rangle - i|A_2\rangle)\chi_{1/2} + (-|B_1\rangle + i|B_2\rangle)\chi_{-1/2}, \quad (8)$$

$$\psi_{-1/2} = (|B_1\rangle + i|B_2\rangle)\chi_{1/2} + (|A_1\rangle + i|A_2\rangle)\chi_{-1/2}, \quad (9)$$

where A_1, A_2, B_1, B_2 label the symmetry type of the spatial part, and $\chi_{1/2}$ and $\chi_{-1/2}$ denote the up and down electron spinor.

The eigenstates of the spin-orbit coupled Hamiltonian are again solved via the ISE method as described in step 2. Each state is twofold due to the Kramer's degeneracy and the two degenerate states are related by applying the time-reversal operator. In this step, the wave functions become complex. However, the CPU time required to get convergent results is comparable to that in step 2, since the spin-orbit interaction only mixes different spin states on the same orbital site, so the multiplication of U or V by the eigenvector C can be performed efficiently. The material parameters used in the present calculation are listed in Table I.

III. RESULTS AND DISCUSSIONS

A. Strain distributions

Strain distributions in four SAQD's with base length $b = 125, 158, 204,$ and 250 \AA plus a truncated pyramidal dot are calculated via VFF model as described in Sec. II. Figure 1 shows a schematic plot of a pyramidal QD on a wetting layer. The GaAs capping layer is not shown. We use a large supercell to model an isolated QD. The supercell size for the four dots considered here is $36a \times 36a \times 21a$, $42a \times 42a \times 24a$, $50a \times 50a \times 28a$, and $58a \times 58a \times 32a$, where a is the lattice constant of bulk GaAs ($a = 5.6533 \text{ \AA}$). In all our calculations the wetting layer is set to be one monolayer (ML) of InAs.

Considering that strain is much stronger near the interfaces, we shall investigate the strain distribution in these dots along a tangential line parallel to one of the dot borders in a plane normal to z (line B in Fig. 1). For comparison, we also investigate the strain distribution along a primary axis through the center in the same plane (line A in Fig. 1). The confinement induced by the strain is determined by the strain Hamiltonian H_{st} plus the piezoelectric potential V_p , since the presence of shear strain can induce a piezoelectric charge in zinc-blende semiconductors. The off-diagonal elements of the strain Hamiltonian are relatively small and less significant and the confinement effect on the wave function prima-

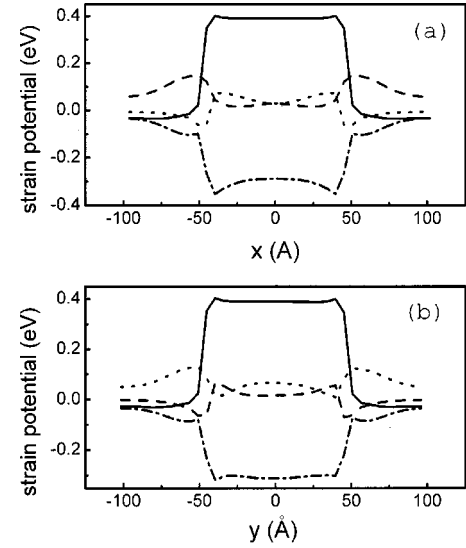


FIG. 2. Diagonal elements of the strain potential of dot 1 in the plane of 17 \AA from dot base (a) along the x direction with $y=0$ (A line as shown in Fig. 1) and (b) along the y direction with $b/2 - 17 \text{ \AA}$ (B line as shown in Fig. 1). The solid line is for V_{ss} , dashed line for V_{xx} , dotted line for V_{yy} , and dot-dashed line for V_{zz} .

rially comes from the diagonal elements. Figures 2 and 3 show the diagonal elements of the strain Hamiltonian (H_{st}) for dots 1 and 5 along lines A and B. Here $V_{ss} = c_1(e_{xx} + e_{yy} + e_{zz})$, $V_{xx} = -\Delta V_H + D_1$, $V_{yy} = -\Delta V_H + D_2$, and $V_{zz} = -\Delta V_H + D_3$. Also, $\Delta V_H, D_1, D_2,$ and D_3 are defined in Sec. II B. The strain distribution at the interface and along primary axes is similar for dots of different sizes, but the strain distribution in the interior of dot is quite different. From these figures, we see that the hydrostatic strain is approximately uniform throughout the dot. The primary effect of the biaxial strain distribution is that in the large dot (dot 5) the

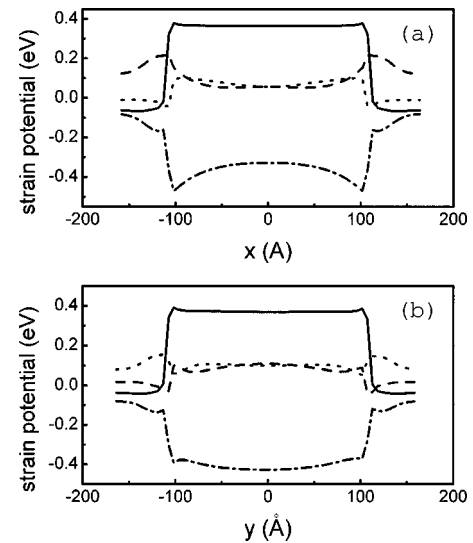


FIG. 3. Diagonal elements of the strain potential of dot 5 in the plane of 17 \AA from dot base (a) along the x direction with $y=0$ (A line as shown in Fig. 1) and (b) along the y direction with $b/2 - 17 \text{ \AA}$ (B line as shown in Fig. 1). The solid line is for V_{ss} , dashed line for V_{xx} , dotted line for V_{yy} , and dot-dashed line for V_{zz} .

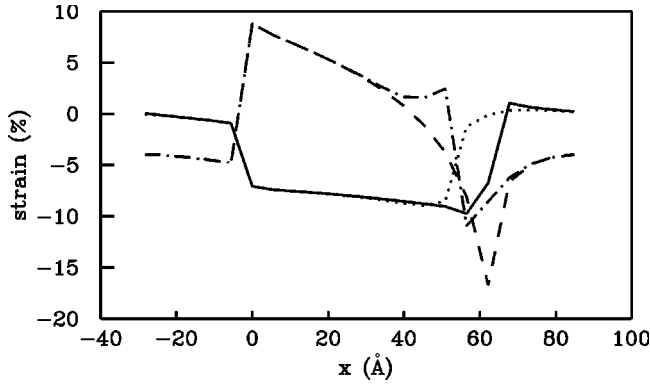


FIG. 4. Strain distribution along [001] of dot 1 and dot 2. The solid line and dot line are for the hydrostatic strain of dot 1 and dot 2, dashed line and dot-dashed line for the biaxial strain of dot 1 and dot 2.

strain potential V_{xx} near the interface has a maximum at the center of line B (with $x = 17 \text{ \AA}$ from the dot border), while in the small dot it has maxima at the corners of the dot. The qualitative difference in the strain distribution can cause a dramatic change in the hole charge density distribution in dot 5 in comparison to dots 1–4 as will be discussed in Sec. III B.

Figure 4 shows the strain distribution along the z axis for dots 1 and 2. For dot 2 (truncated pyramid), the strain distribution is different from that in dot 1 only near the truncated top of the pyramid as shown in Fig. 4. Since the wave function of the ground state for an electron or hole are predominantly localized near the base area of the dot, we expect the photoluminescence property of the truncated pyramid to be very similar to that in the pyramidal dot of the same base length. This will be reflected in the interband optical matrix elements shown in Sec. III B.

As indicated earlier by Grundmann *et al.*²³ the piezoelectric potential V_p is significant at dot borders along [110] and $[1\bar{1}0]$ and the signs of V_p along these two directions are opposite. Thus the envelope functions with and without the piezoelectric effect are quite different as will be shown in the next section, even though their energy levels are fairly close. The maximum values of $|V_p|$ for dots 1, 3, 4, and 5 are 50.4, 60.7, 73.1, and 85.0 meV, respectively.

B. Electronic structures

The strain Hamiltonian H_{st} and piezoelectric potential V_p plus band offsets determine the quantum confinement of wave functions. In order to investigate the effects of H_{st} and V_p , we first study the electronic structures by leaving out V_p ; we then study the effect of the piezoelectric potential by adding V_p . The energies of the four low-lying conduction-band states and four high-lying valence-band states vs dot size are shown in Fig. 5.

Without the strain effects, the confinement of electron or hole is determined by the corresponding band offset (see Table I). Namely, in the InAs region, the electron sees a potential well with depth 0.833 eV while the hole sees a potential well with depth 0.26 eV.⁴³ Including the diagonal elements of H_{st} , the net potential profile seen by an electron or hole is described by the curves shown in Figs. 2 and 3

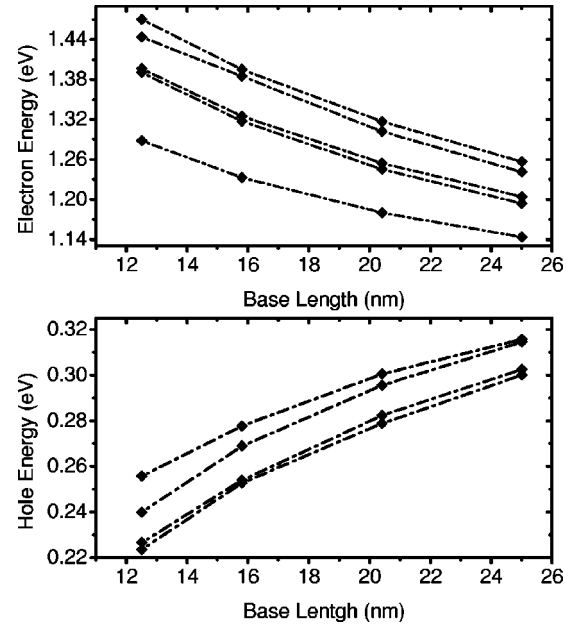


FIG. 5. Energy levels of the four lowest-lying conduction bands and the highest-lying valence bands vs dot size.

plus the effects of the corresponding band offsets. Due to the presence of biaxial strain, different components of the hole states experience different potential profiles. For example, at the center of line B in dot 5 the x component of hole states is subject to a confining potential of a height around 0.36 eV (0.1 eV due to V_{xx} plus 0.26 eV due to the VB offset) and the z component of hole states is not confined, since $V_{zz} = -0.4$ eV, which overcomes the 0.26 eV VB offset. Thus, based on the information provided in Figs. 2 and 3, we can conclude that the confined hole states in SAQD's are predominantly linear combinations of x -like and y -like bond orbitals.

Since the hydrostatic strain distribution is approximately uniform in all dots, the ground-state wave functions and charge density distributions for electrons in these dots are qualitatively similar and they are all peaked near the center of the dot. The piezoelectric effect on wave functions of low-lying electron states are very small since the piezoelectric potential is much smaller than the confinement potential determined by the strain potential and band offset. Moreover, the effect of the spin-orbit interaction is weak, and each electron state has a predominant component which transforms according the irreducible representations of the C_{2v} point group. Figure 6 shows contour plots of charge density distributions for the first four conduction-band states (CB1–4) of dot 1 in the plane with $z = 17 \text{ \AA}$ from the base. Our results of electronic levels and charge density distributions agree well with the $\mathbf{k} \cdot \mathbf{p}$ calculations of Stier *et al.*²⁶

For valence-band states, without the piezoelectric effect the hole wave functions and charge density distributions are sensitive to the dot size due to a different biaxial strain distribution. In particular, the hole charge density distribution of dot 5 is quite different from that of dots 1–4. Figure 7 shows the contour plots of charge density distributions for the hole ground states (VB1) of dots 1 and 5 in the plane with $z = 17 \text{ \AA}$ from the dot base. We can see that the VB1 charge density of dot 1 is concentrated along the [110] diagonal line

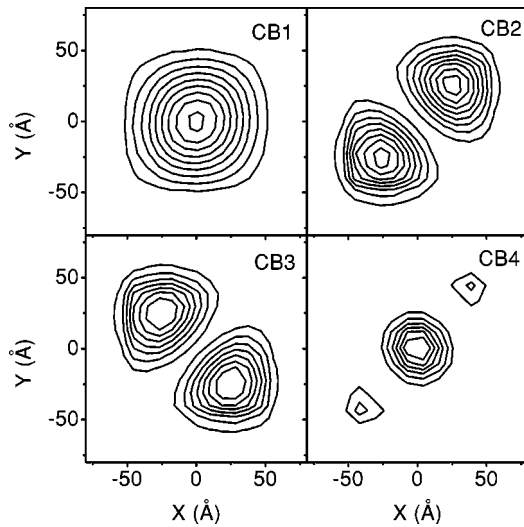


FIG. 6. Contour plots of the charge density distributions for states CB1–4 (with piezoelectric effect) for dot 1 in a plane at $z = 17 \text{ \AA}$ from the dot base.

of the dot and it has an appreciable amplitude near the center. For dot 5 the charge density is peaked at the center of tangential lines near the dot borders (line B and the equivalent lines due to point-group symmetry) and it has very small amplitude near the center of the dot. Due to the strong spin-orbit coupling, no predominant symmetry type of hole envelope functions can be identified.

Next, we consider the effects of the piezoelectric potential (V_p). We found that the inclusion of V_p can distort the hole wave functions substantially as shown in Fig. 8 for the top four valence-band states (VB1–4) of dots 1 and 5. The

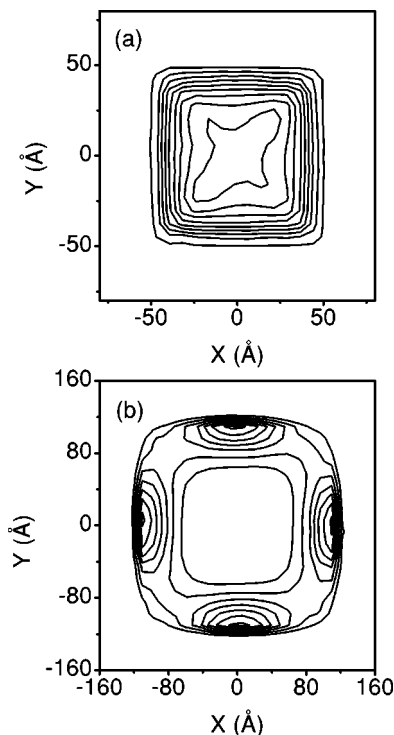


FIG. 7. Contour plots of the charge density distributions for the ground hole state (without the piezoelectric effect) in a plane at $z = 17 \text{ \AA}$ from the dot base for (a) dot 1 and (b) dot 5.

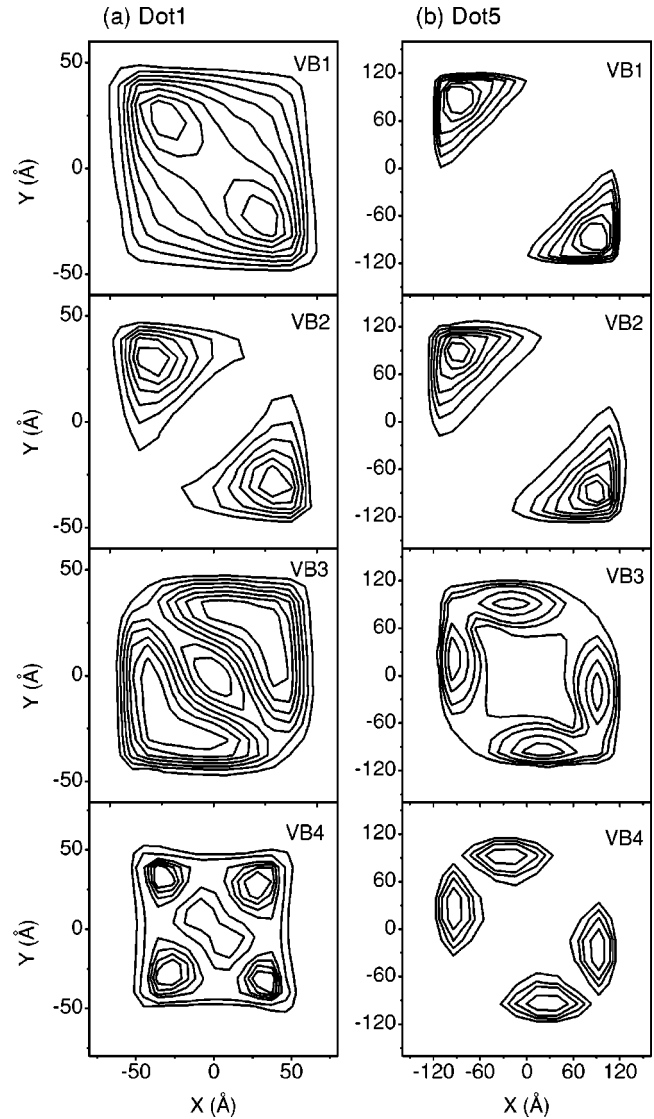


FIG. 8. Contour plots of the charge density distributions for states VB1–4 (with the piezoelectric effect) in a plane at $z = 17 \text{ \AA}$ from the dot base for (a) dot 1 and (b) dot 5.

charge densities for all four hole levels are stretched along the $[1\bar{1}0]$ axis, which can be seen by comparing Fig. 7 with Fig. 8 for ground holes. This change in the hole charge density distribution leads to substantially different interband optical properties with and without the piezoelectric effect. Comparing our results and those of Steir *et al.*, good coincidence can be seen. However, the energy difference between the corresponding electron and hole states is smaller than that of Stier *et al.* This is mainly due to the different deformation potentials in our paper, which are taken from Ref. 25.

Investigating the various components of wave functions, it can be seen that electron wave functions contain predominantly an s component (around 90%), while hole wave functions for the top four VB states contain primarily x and y components (or bond characters), indicating that they are mainly derived from the heavy-hole band. As pointed out by others, the envelope function for the ground state (CB1) is s -like, while the envelope functions for excited states (CB2–CB4) are p -like.

TABLE II. Interband transition energies (in eV) and the corresponding overlap integrals between the s component of the electron state and the x' , y' , and z components of hole states with and without the piezoelectric effect. Values in parentheses are results with the piezoelectric effect.

Dot No.	Hole state index	ΔE (eV)	$\langle s x'\rangle^2$	Overlap $\langle s y'\rangle^2$	$\langle s z\rangle^2$
Dot 1 $b=125 \text{ \AA}$ $h=0.5 b$	VB1	1.0355 (1.0322)	0.314 (0.329)	0.333 (0.299)	0.0 (0.0)
	VB2	1.0508 (1.0480)	0.0 (0.0)	0.001 (0.002)	0.0 (0.0)
	VB3	1.0606 (1.0612)	0.027 (0.015)	0.024 (0.039)	0.049 (0.045)
	VB4	1.0649 (1.0643)	0.004 (0.001)	0.005 (0.023)	0.0 (0.0)
Dot 2 $b=125 \text{ \AA}$ $h=0.4 b$	VB1	1.0341 (1.0328)	0.317 (0.331)	0.335 (0.303)	0.0 (0.0)
	VB2	1.0514 (1.0489)	0.0 (0.0)	0.0 (0.003)	0.0 (0.0)
	VB3	1.0624 (1.0627)	0.025 (0.014)	0.023 (0.042)	0.044 (0.040)
	VB4	1.0656 (1.0652)	0.005 (0.002)	0.006 (0.017)	0.0 (0.0)
Dot 3 $b=158 \text{ \AA}$ $h=0.5 b$	VB1	0.9574 (0.9550)	0.298 (0.302)	0.312 (0.249)	0.0 (0.0)
	VB2	0.9679 (0.9636)	0.0 (0.0)	0.0 (0.003)	0.0 (0.003)
	VB3	0.9790 (0.9786)	0.0 (0.016)	0.0 (0.030)	0.008 (0.0)
	VB4	0.9791 (0.9798)	0.19 (0.003)	0.021 (0.043)	0.030 (0.032)
Dot 4 $b=204 \text{ \AA}$ $h=0.5 b$	VB1	0.8856 (0.8810)	0.252 (0.228)	0.261 (0.167)	0.0 (0.0)
	VB2	0.8905 (0.8844)	0.002 (0.0)	0.002 (0.003)	0.0 (0.003)
	VB3	0.8981 (0.8977)	0.001 (0.037)	0.003 (0.059)	0.0 (0.0)
	VB4	0.9010 (0.9012)	0.009 (0.004)	0.010 (0.012)	0.025 (0.019)
Dot 4 $b=250 \text{ \AA}$ $h=0.5 b$	VB1	0.8352 (0.8274)	0.192 (0.148)	0.197 (0.100)	0.0 (0.0)
	VB2	0.8369 (0.8284)	0.004 (0.0)	0.005 (0.004)	0.0 (0.002)
	VB3	0.8417 (0.8326)	0.0 (0.054)	0.002 (0.054)	0.0 (0.0)
	VB4	0.8452 (0.8431)	0.004 (0.001)	0.004 (0.004)	0.013 (0.009)

We also calculated the electron and hole states of truncated pyramidal dot (dot 2). We found that the energy shifts in low-lying levels in comparison with untruncated pyramidal dots are insignificant. This is because the wave functions of these electron or hole states are primarily localized near the base of the dot, where the truncation of the pyramid tip has little effect.

The exciton states of SAQD's can be calculated via a self-consistent method (Hartree approximation) as adopted in Ref. 26. The exciton state is written as a product of electron and hole states $\Psi_X = \phi_e \phi_h$ and each one-particle state satisfies the self-consistent Schrödinger equation

$$(H_e + \langle \phi_h | v_{eh} | \phi_h \rangle) \psi_e = E_e \psi_e,$$

$$(H_h + \langle \phi_e | v_{eh} | \phi_e \rangle) \psi_h = E_h \psi_h,$$

where $H_e(H_h)$ is the electron (hole) one-particle Hamiltonian and v_{eh} is the electron-hole Coulomb interaction. To solve the above self-consistent equations, we use the ground-state wave function (in the bond-orbital basis) for the electron or hole as the initial guess. We then obtain the electron charge density via the relation (and similarly for the hole)

$$\rho_e(\mathbf{R}) = \sum_{\alpha} |C_{\alpha}^{CB1}(\mathbf{R})|^2,$$

where $C_{\alpha}^{CB1}(\mathbf{R})$ is the expansion coefficient of the CB1 state in terms of a bond orbital of type α at site \mathbf{R} . The electron-hole interaction seen by the hole at site \mathbf{R}_2 is then given by

$$\langle \phi_e | v_{eh} | \phi_e \rangle = - \sum_{\mathbf{R}_1} \rho_e(R_1) \frac{e^2}{\epsilon_0 |R_1 - R_2|} \quad \text{for } \mathbf{R}_1 \neq \mathbf{R}_2,$$

where e is the electron charge and ϵ_0 is the static dielectric constant. Here, we have used the fact that the bond orbitals are orthogonal to each other and the Coulomb potential $e^2/\epsilon_0 r_{12}$ is a smooth function of r_1 , so we can replace it at the discrete site R_1 . Due the singularity of the Coulomb interaction at the origin (when $\mathbf{R}_1 = \mathbf{R}_2$), we approximate the denominator r_{12} by the average electron-hole distance within a bond orbital, r_0 , which is taken to be half of the bond length. We found that since the on-site Coulomb matrix element is only a small fraction (less than 1%) of the sum, the exact value of r_0 is of little importance. Adding the electron-hole interaction to the one-particle Hamiltonian H_h , we can then find the new hole wave function ϕ_h for the exciton following the same procedure as described in Sec. II B. The procedure is then repeated for the electron to find the new wave function ϕ_e . After just a couple iterations, the exciton binding energy defined as $E_e + E_h - (E_{CB1} - E_{VB1})$ can be obtained with an accuracy better than 0.1 meV. For the four pyramidal dots the calculated exciton binding energies are 26.1 meV, 20.5 meV, 15.8 meV, 11.8 meV. These values are consistent in magnitude with those reported in Ref. 26.

C. Optical properties

The optical properties of interest include the interband transitions (between conduction-band and valence-band states) and intraband transitions (between QD states derived from the conduction band). InAs SAQD's on GaAs(001) have been studied by a number of authors^{12–18} via photoluminescence (PL) and cathode luminescence (CL) spectroscopy. Due to size fluctuation, the excited-state spectrum is difficult to assign unambiguously. Recently, photoluminescence excitation (PLE) spectroscopy was used to study this issue.¹⁷ Here we present the results of our calculations on ideal homogeneous SAQD's, although a quantitative comparison between theory and experiment is difficult due to size fluctuations.

For interband transitions, the linear absorption coefficient within the dipole approximation is proportional to the overlap between electron and hole states. The overlap integrals are defined as

$$|\langle s|\alpha\rangle|^2 = \left| \sum_{\mathbf{R}} C_s^{i*}(\mathbf{R}) C_\alpha^f(\mathbf{R}) \right|^2, \quad \alpha = x', y', z,$$

where the superscripts i and f label the initial and final states, x' is along $[1\bar{1}0]$, y' along $[110]$, and z long $[001]$. In Table II we list the energy differences between ground electron state (CB1) and top four valence states (VB1–4) and the corresponding electron-hole overlap integrals. The results which take into account the piezoelectric effect are listed in parentheses. Without the piezoelectric effect the optical transition from the ground electron to ground hole state is polarized along the y' direction, and the degree of polarization reduces with increasing dot size. With the piezoelectric potential included the interband optical transitions for all dots become polarized along the x' direction, and the degree of polarization increases with increasing dot size. This is caused by the fact that the piezoelectric potential tends to stretch the hole wave functions along the x' direction as seen in Fig. 8. Tang *et al.*¹⁸ studied the polarization anisotropy of InAs/GaAs(001) SAQD's by CL and their results indicate that the ratio of x' to y' polarization is around 1.17 for the fundamental (P1) transition in QD's with an average base length of 15 nm. This result is very close to our result of dot 3 (around 1.2). It should be noted that for all dots considered, the z -component optical transition is negligible. We can see that the electron-hole overlap integrals of dot 5 are more than a factor 2 smaller than those of dot 1. This is due to the fact that in dot 5 the hole wave function is distributed away from the center of the dot (see Fig. 8), while the electron ground-state (CB1) wave function is concentrated at the center of the dot. Consistent with the above discussions on the truncation of the pyramid, the overlap integrals of dot 1 and dot 2 are approximately the same.

For intraband transitions, the optical matrix element is proportional to the dipole matrix element, since

$$\langle i|[\mathbf{r}, H]|f\rangle = (E_i - E_f) \langle i|\mathbf{r}|f\rangle = \frac{i\hbar}{m} \langle i|\mathbf{p}|f\rangle,$$

where the superscripts i and f label the initial and final states. Within the bond-orbital basis, the dipole matrix elements can be approximated by

TABLE III. Dipole matrix elements for transitions from the electron ground state (CB1) to excited states (CB2–4), $|\langle \phi_{1,c}|\mathbf{r}|\phi_{i,c}\rangle|^2$. Polarization direction is either x ($=y$) or z . Values in parentheses are results with the piezoelectric effect.

Dot No.	Electron state i	ΔE (eV)	x	z
Dot 1	CB2	0.1053	300.8 (308.5)	0.0 (0.0)
	CB3	0.1060	297.7 (292.5)	0.0 (0.0)
	CB4	0.1563	0.0 (0.0)	18.3(18.9)
Dot 3	CB2	0.0885	383.9 (400.1)	0.0 (0.0)
	CB3	0.0890	379.6 (367.8)	0.0 (0.0)
	CB4	0.1565	0.0 (0.0)	1.6 (29.9)
Dot 4	CB2	0.0698	536.5 (573.8)	0.0 (0.0)
	CB3	0.0702	531.0 (501.4)	0.0 (0.0)
	CB4	0.1257	0.0 (0.0)	1.1 (32.4)
Dot 5	CB2	0.0558	725.3 (798.7)	0.0 (0.0)
	CB3	0.0562	717.2 (660.4)	0.0 (0.0)
	CB4	0.1020	0.0 (0.0)	0.2 (36.7)

$$\langle i|\mathbf{r}|f\rangle = \sum_{\mathbf{R}, \alpha} C_\alpha^{i*}(\mathbf{R}) C_\alpha^f(\mathbf{R}) \mathbf{R}.$$

In Table III, the dipole matrix elements squared for x , y , and z polarizations are listed for intraband transitions from the ground electron state (CB1) to upper electron states (CB2–4). The intraband transition energies are also listed. It can be seen that the dipole matrix elements for x and y polarizations for CB1-CB2 and CB1-CB3 transitions are significant. This means that light with normal incidence (along z) can be directly absorbed via the CB1-CB2 and CB1-CB3 intraband transitions. In comparison, the n -type quantum well infrared photodetectors (QWIP's) usually require special processing (e.g., surface grating) to allow normal incident light to couple with electronic intersubband transitions.⁴⁵ In this aspect, the SAQD's have an advantage over quantum wells for infrared detector applications.

Finally, we calculate the dipole moment induced by the intraband optical absorption. Because the charge distributions in the excited states are very different from the electron ground state (CB1), we expect a large optical-induced dipole moment for SAQD's. This feature may be utilized for applications in photovoltaic devices. We define the optical-induced dipole moment for the intraband transitions from the CB1 state the CB i excited state ($i=2, \dots, 4$) by

$$\mathbf{p}_i = \sum [\rho_{CBi}(\mathbf{R}) - \rho_{CB1}(\mathbf{R})] \mathbf{R},$$

where $\rho_{CBi}(\mathbf{R}) = \sum_\alpha |C_\alpha^{CBi}(\mathbf{R})|^2$. As shown in Table IV, the dipole moments of the three intraband transitions increase with dot size.

IV. SUMMARY

We have presented a systematic study of the electronic and optical properties of self-assembled quantum dots of different sizes via an efficient order- N numerical method based

TABLE IV. Optical-induced dipole moment $\mathbf{p}_i = \Sigma[\rho_{CBi}(\mathbf{R}) - \rho_{CB1}(\mathbf{R})]\mathbf{R}$ in units of $e \text{ \AA}$. Only the p_z component is listed. The p_x and p_y components are negligibly small. Values in parentheses are results with the piezoelectric effect.

	Dot 1	Dot 3	Dot 4	Dot 5
CB1-CB2	-4.34 (-4.92)	-4.93 (-5.36)	-5.50 (-5.99)	-5.90 (-6.31)
CB1-CB3	-4.33 (-3.63)	-4.92 (-4.26)	-5.47 (-4.92)	-5.90 (-5.40)
CB1-CB4	-4.74 (-4.89)	-7.40 (-6.35)	-8.41 (-6.96)	-9.24 (-7.49)

on the effective bond-orbital model. Microscopic strain distributions have been taken into account within the valence-force-field model and the piezoelectric effect induced by shear strain has also been studied. We first studied the effect of quantum confinement and strain without including the piezoelectric effect. We found that the strain distribution is sensitive to the size of SAQD's, and it can lead to different electronic and optical properties. For all dots considered, the hydrostatic strain is approximately uniform within the dot in a plane normal to the growth (z) axis and it has a nearly constant slope along the z axis. When the dot size increases to a certain value (with base length around 250 \AA), the maxima of the x or y component of the biaxial strain potential move from the corners of the dot to the centers of the dot borders. Due to this change in the strain distribution, the ground-hole-state charge density distribution is quite different in the large dot compared with those in smaller dots and leads to a much weaker polarization in the interband optical transition for large dots. Furthermore, in the large dot, the hole charge density is distributed away from the center of the dot, causing a substantial reduction in the electron-hole overlap and hence a much weaker interband transition matrix element. By including the piezoelectric effect we found that the energy levels only shift slightly but the valence-band charge density distribution and interband optical transitions are modified substantially. All the hole wave functions are stretched along the $[1\bar{1}0](x')$ axis and hence the interband

optical transitions become polarized along the $[1\bar{1}0]$ direction and the polarization ratio increases with dot size. This finding is consistent with the experiment.¹⁸

We have also calculated the intraband transitions for the conduction-band states and we found that the CB1-CB2 and CB1-CB3 transitions in all dots considered here have strong dipole transition strengths for the transverse polarizations (x and y) of the normal-incidence light and the transition energies are in the range of $0.05\text{--}0.1 \text{ eV}$. Thus, the SAQD's considered are suitable for far-infrared detector applications. We also found that the SAQD's considered here can have a strong z -component optical-induced dipole moment, which may find applications in photovoltaic devices.

The exciton states have also been studied within the Hartree approximation. For smaller dots (with base length less than 200 \AA), our EBOM results on energy levels, charge distributions, and exciton binding energies are in good agreement with previous $\mathbf{k}\cdot\mathbf{p}$ calculations.²⁶

ACKNOWLEDGMENTS

This work was supported by a subcontract from the University of Southern California under the MURI program, AFOSR, Contract No. F49620-98-1-0474. We would like to thank Zhonghui Chen for pointing out the large optical-induced dipole moments in SAQD's.

¹K.W. Berryman, S.A. Lyon, and M. Segev, *Appl. Phys. Lett.* **70**, 1861 (1997).

²S. Sauvage, P. Boucaud, F.H. Julien, J.-M. Gerard, and V. Thierry-Mieg, *Appl. Phys. Lett.* **71**, 2785 (1997).

³Q. Xie, A. Kalburge, P. Chen, and A. Madhukar, *IEEE Photonics Technol. Lett.* **8**, 965 (1996).

⁴N.N. Lednstov, M. Grundmann, N. Kirstaedter, O. Schmidt, R. Heitz, J. Böhrer, D. Bimberg, V.M. Ustinov, V.A. Shchukin, A.Yu. Egorov, A.E. Zhukov, S. Zaitsev, P.S. Kop'ev, Zh.I. Alferov, S.S. Ruvimov, A.O. Kosogov, P. Werner, U. Gösele, and J. Heydenreich, *Solid State Electron.* **40**, 785 (1996).

⁵S. Guha, A. Madhukar, and K.C. Rajikumar, *Appl. Phys. Lett.* **57**, 2110 (1990).

⁶D.J. Eaglesham and M. Cerullo, *Phys. Rev. Lett.* **64**, 1943 (1990).

⁷G.S. Solomon, J.A. Trezza, A.F. Marshall, and J.S. Harris, Jr., *Phys. Rev. Lett.* **76**, 952 (1996).

⁸J. Tersoff, C. Teichert, and M.G. Lagally, *Phys. Rev. Lett.* **76**, 1675 (1996).

⁹V. Holy, G. Springholz, M. Pinczolit, and G. Bauer, *Phys. Rev. Lett.* **83**, 356 (1999).

¹⁰M.G. Alessi, M. Capizzi, A.S. Bhatti, A. Frova, F. Martelli, P. Frigeri, A. Bosacchi, and S. Franchi, *Phys. Rev. B* **59**, 7620 (1999).

¹¹R. Cingolani, R. Rinaldi, H. Lipsanen, M. Sopanen, R. Virkkala, K. Majjala, J. Tulkki, J. Ahopelto, K. Uchida, N. Miura, and Y. Arakawa, *Phys. Rev. Lett.* **83**, 4832 (1999).

¹²M. Grundmann, J. Christen, N.N. Lednstov, J. Böhrer, D. Bimberg, S.S. Ruvimov, P. Werner, U. Richter, U. Gösele, J. Heydenreich, V.M. Ustinov, A.Yu. Egorov, A.E. Zhukov, P.S. Kop'ev, and Zh.I. Alferov, *Phys. Rev. Lett.* **74**, 4043 (1995).

¹³J.-Y. Marzin, J.-M. Gerard, A. Izrael, and D. Barrier, *Phys. Rev. Lett.* **73**, 716 (1994).

¹⁴F. Alder, M. Geiger, A. Bauknecht, F. Schilz, H. Schweizer, and M.H. Pilkuhn, *J. Appl. Phys.* **80**, 4019 (1996).

¹⁵K.H. Schmidt, G. Medeiros-Ribeiro, M. Oestreich, and P.M. Petroff, *Phys. Rev. B* **54**, 11 346 (1996).

¹⁶F. Fafard, R. Lenon, D. Leonard, J.L. Merz, and P.M. Petroff, *Phys. Rev. B* **52**, 5752 (1995).

¹⁷R. Heitz *et al.*, *Appl. Phys. Lett.* **68**, 361 (1996); R. Heitz *et al.*, *Physica E (Amsterdam)* **2**, 578 (1998); R. Heitz, I.

- Mukhametzhanov, O. Stier, A. Madhukar, and D. Bimberg, *Phys. Rev. Lett.* **83**, 4654 (1999).
- ¹⁸Y. Tang, D.H. Rich, I. Mukhametzhanov, P. Chen, and A. Madhukar, *J. Appl. Phys.* **84**, 3342 (1998).
- ¹⁹J.-Y. Marzin and G. Bastard, *Solid State Commun.* **92**, 437 (1994).
- ²⁰M.A. Cusack, P.R. Briddon, and M. Jaros, *Physica B* **253**, 10 (1998).
- ²¹S.S. Li and J.-B. Xia, *Phys. Rev. B* **55**, 15 434 (1997).
- ²²L.W. Wang, J. Kim, and A. Zunger, *Phys. Rev. B* **59**, 5678 (1999).
- ²³M. Grundmann, O. Stier, and D. Bimberg, *Phys. Rev. B* **52**, 11 969 (1995).
- ²⁴C. Pryor, *Phys. Rev. B* **57**, 7190 (1998).
- ²⁵H. Jiang and J. Singh, *Phys. Rev. B* **56**, 4696 (1997).
- ²⁶O. Stier, M. Grundmann, and D. Bimberg, *Phys. Rev. B* **59**, 5688 (1999).
- ²⁷W. Yang, H. Lee, T. Johnson, and P.C. Sereel, *Phys. Rev. B* **61**, 2784 (2000).
- ²⁸D. Gammon, E.S. Snow, B.V. Shanabrook, D.S. Katzer, and D. Park, *Science* **273**, 87 (1996); *Phys. Rev. Lett.* **76**, 3005 (1996).
- ²⁹F. Gindele, K. Hild, W. Langbein, and U. Woggon, *Phys. Rev. B* **60**, R2157 (1999), and references therein.
- ³⁰Y.C. Chang, *Phys. Rev. B* **37**, 8215 (1988).
- ³¹M.-P. Houg and Y.C. Chang, *J. Appl. Phys.* **65**, 3092 (1989).
- ³²D.S. Citrin and Y.C. Chang, *J. Appl. Phys.* **68**, 161 (1990).
- ³³L. Li and Y. C. Chang, *J. Appl. Phys.* **84**, 6162 (1998).
- ³⁴C. Pryor, J. Kim, L.W. Wang, A.J. Williamson, and A. Zunger, *J. Appl. Phys.* **83**, 2548 (1998).
- ³⁵P.N. Keating, *Phys. Rev.* **145**, 637 (1966).
- ³⁶R. Martin, *Phys. Rev. B* **1**, 4005 (1970).
- ³⁷J.W. Matthews and A.E. Blakeslee, *J. Cryst. Growth* **27**, 18 (1974).
- ³⁸G.C. Osbourn, *Phys. Rev. B* **27**, 5126 (1983).
- ³⁹G.L. Bir and G.E. Pikus, *Symmetry and Strain Induced Effects in Semiconductors* (Wiley, Halsted, UK, 1974); L.D. Landau and E.L. Lifshitz, *Theory of Elasticity* (Addison-Wesley, Reading, MA, 1970).
- ⁴⁰M. Tinkham, *Group Theory and Quantum Mechanics* (McGraw-Hill, New York, 1964).
- ⁴¹D.J. Chadi, *Phys. Rev. B* **16**, 790 (1977).
- ⁴²G.F. Koster, J.O. Dimmock, R.G. Wheeler, and H. Statz, *Properties of the Thirty-two Point Groups* (MIT Press, Cambridge, MA, 1963).
- ⁴³Ch.G. Van der Walle, *Phys. Rev. B* **39**, 1871 (1989).
- ⁴⁴*Numerical Data and Functional Relationships in Science and Technology*, edited by O. Madelung, Landolt-Börnstein, New Series, Group III, Vol. 22a, Pt. 17A. (Springer, Berlin, 1982).
- ⁴⁵*Semiconductor Quantum Wells and Superlattices for Long-Wavelength Infrared Detectors*, edited by M. O. Manasreh (Artech House, Boston, 1993).